Simulation of a low-Z-medium detector for low-dose high-resolution TOF-PET

Kepler Domurat-Sousa, Cameron M. Poe, Maya S. McDaniel, Eric Spieglan, Joao F. Shida, Evan Angelico, Bernhard W. Adams, Patrick J. La Riviere, Henry J. Frisch, and Allison H. Squires

***Abstract*—**Two major challenges in time-of-flight positron emission tomography (TOF-PET) are low spatial resolution and high radioactive dose to the patient, both of which result from limitations in detection technology rather than fundamental physics. A new type of TOF-PET detector employing low-atomic number (low-Z) scintillation media and large-area, high-resolution photodetectors to record Compton scattering locations in the detector has been proposed as a promising alternative, but neither a direct comparison to state-of-the-art TOF-PET nor the minimum technical requirements for such a system have yet been established. Here we present a simulation study evaluating the potential of a proposed low-Z detection medium, linear alkylbenzene (LAB) doped with a switchable molecular recorder, for next-generation TOF-PET detection. We developed a custom Monte Carlo simulation of full-body TOF-PET using the TOPAS Geant4 software package. By quantifying contributions and tradeoffs for energy, spatial, and timing resolution of the detector, we show that a reasonable combination of specifications improves TOF-PET sensitivity by more than 5x, with comparable or better spatial resolution and 40-50% enhanced contrast-to-noise as compared to state-of-the-art scintillating crystal materials. These improvements enable clear imaging of a brain phantom simulated at less than 1% of a standard radiotracer dose, which could enable expanded access and new clinical applications for TOF-PET.

***Index Terms*—**Geant4, photoswitchable fluorophore, positron emission tomography, TOF-PET, TOPAS.

I. INTRODUCTION

TIME-OF-FLIGHT Positron Emission Tomography (TOF-PET) provides critical medical insights into the metabolic and biochemical function of tissues and organs by mapping relative uptake of a positron-emitting radiotracer. TOF-PET imaging traditionally relies on detecting coincident pairs of gamma photon arrivals recorded by scintillation crystals arrayed around the subject. Despite its high sensitivity and biological specificity, the major drawbacks of TOF-PET remain (1) low image resolution of several mm due to the precision with which gamma photon trajectories are determined, setting the minimum detectable size of features such as cancer metastases [1], [2], and (2) low detector sensitivity such that only 1-2% of

Manuscript received Xxxxxxxx XX, XXXX; revised Xxxxxxxx XX, XXXX; accepted Xxxxxxxx XX, XXXX. Date of publication Xxxxxxxx XX, XXXX.This work was supported in part by NIH R01EB026300 to P. J. La Riviere, a Neubauer Family Foundation award and a University of Chicago MRSEC seed grant (NSFDMR-2011854) to A. H. Squires, funding from the University of Chicago College, Physical Sciences Division and Enrico Fermi Institute to K. Domurat-Sousa, C. Poe, and J. F. Shida, and a University of Chicago Quad Undergraduate Research Scholarship to M. S. McDaniel.

K. Domurat-Sousa, C. Poe, E. Spieglan, and H. J. Frisch are with the Enrico Fermi Institute, University of Chicago, Chicago, IL 60637 USA; J. F. Shida and E. Angelico were with the Enrico Fermi Institute and are now respectively with the Department of Chemistry, MIT, Cambridge, MA 01239 USA, and the Department of Physics, Stanford University, Stanford, CA 94305. (e-mail: domuratsousa@uchicago.edu; cameronpoe@uchicago.edu; jshida@mit.edu; eangelic@stanford.edu; eric.spieglan@gmail.com; frisch@hep.uchicago.edu).

B. W. Adams is with Quantum Optics Applied Research, Naperville, IL 60564 USA (e-mail: bwa@uchicago.edu).

M. S. McDaniel and A. H. Squires are with the Pritzker School of Molecular Engineering, University of Chicago, Chicago, IL 60637 USA; A. H. Squires is also with the Institute for Biophysical Dynamics at the University of Chicago (e-mail: msmcdaniel@uchicago.edu; asquires@uchicago.edu).

P. J. La Riviere is with the Department of Radiology at the Pritzker School of Medicine, University of Chicago, Chicago, IL 60637 USA (e-mail: pjlarivi@uchicago.edu). Correspondence may be directed to hfrisch@uchicago.edu or asquires@uchicago.edu.

emitted gamma rays are detected in standard (non-full-body) commercial PET systems [3], setting the minimum radioactive exposure for patients, the minimum imaging time, and the geographic accessibility of PET. These limitations arise from technical constraints of the detector technology, such as crystal size and scintillation efficiency, rather than underlying physical principles governing positron annihilation and gamma photon emission [4].

State-of-the-art TOF-PET imagers implement a near-optimized version of this traditional detection approach [5]–[8], [3], [9]. Development of full-body PET systems [1], [10], [11], combined with optimization of detector timing precision [12]–[16], trajectory resolution [17], [18], detector material [19]–[21], and image reconstruction algorithms [22], [23] have enhanced the efficiency with which gamma photons are detected to above 15% and provide higher-precision estimates of positron-electron annihilation locations to improve image resolution to < 3 mm [24]. Yet future TOF-PET development may require order-of-magnitude advances in timing precision or an entirely new detector paradigm to overcome the fundamental sensing limitations and cost tradeoffs of scintillation crystal arrays. In this context, we have been exploring possible TOF-PET scanner designs based on development of inexpensive low atomic number (low-Z) scintillating media [25], [26] and microchannel plate photomultiplier tubes (MCP-PMTs) [27]–[29], with low-cost GHz waveform sampling data-acquisition [30].

Here we present Monte Carlo simulations of full-body TOF-PET using the TOPAS Geant4 software package, with which we evaluate the feasibility, minimum technical requirements, and potential advantages of such a low-Z TOF-PET detector approach. We quantify the contributions and tradeoffs for energy, spatial, and timing resolution on PET scan sensitivity and spatial resolution, and compare this performance to simulations of a state-of-the-art scintillation crystal-based TOF-PET detector. Finally, we simulate low-Z TOF-PET imaging of a brain at 10^{-2}-10^{-4} reduced radiotracer dose to illustrate one potential high-impact use case.

II. Compton Detection in Low-Z Media for TOF-PET

The proposed low-Z TOF-PET detection approach, shown schematically in Fig. 1, exploits Compton scattering rather than the photoelectric effect as the fundamental photon-detector interaction. A low-atomic number (low-Z) liquid scintillation medium is used instead of high-atomic number scintillation crystals, making Compton scattering the predominant interaction [31]. Upon scattering, a recoil electron and scintillation light are generated. With each successive Compton scatter, the gamma photon continues to lose energy until it either leaves the detector or is absorbed. The observed geometry and energies of a chain of Compton scatters, together with its counterpart across the detector and timing information from scintillation and/or Cherenkov light, may be used to statistically infer which event occurred first in each chain (inset, Fig. 1). Lines-of-response (LORs) are determined using these likely pairs of first scatters across the subject, from which the original distribution of radiotracer in the subject may be estimated. This approach is fundamentally different from a “Compton camera” [32], [33], which cannot record more than one scatter.

To record a chain of Compton scatters in the detector, energy from each recoil electron must locally alter the recording medium to indicate the position of the scatter. The extent of this change should correlate to and therefore report the energy of the recoil electron and should be optically detectable. The change must persist for sufficient time to record the interaction with high spatial and energetic precision, and the medium should be reset after each measurement. The recording mechanism could be

thermodynamic, as in a bubble chamber, but chemical changes in molecular state or configuration could offer greater sensitivity and opportunities for external control: One such implementation would utilize photoswitchable fluorophores [34]–[36] that can be locally activated by energy from a recoil electron to switch from a native "dark" state to a fluorescence-capable state that may undergo many cycles of excitation and emission, enabling extended-duration recording of the location and number of switched molecules before returning to the dark state, as described previously [26] and depicted in Fig. 1. The simulations performed in the present work are agnostic to the specific recording mechanism, and instead take the efficiency of converting recoil electron energy into a molecular record as a simulated detector parameter for energy resolution.

Regardless of mechanism, a major advantage of a low-Z detection approach to TOF-PET is that estimation of the locations and energies of gamma photon interactions in the detector can be decoupled from timing measurements, so that these aspects of detection may be independently optimized. The low cost and wide availability of low-Z detection media such as organic solvents means that the sensitivity of the detector may also be independently tuned to achieve high stopping power through altering the detector volume. In the following simulations, we employ linear alkylbenzene (LAB) as the low-Z detection medium. LAB has excellent optical clarity at visible wavelengths, high flash point, is low-cost, and has relatively high viscosity at room temperature, limiting solute diffusion.

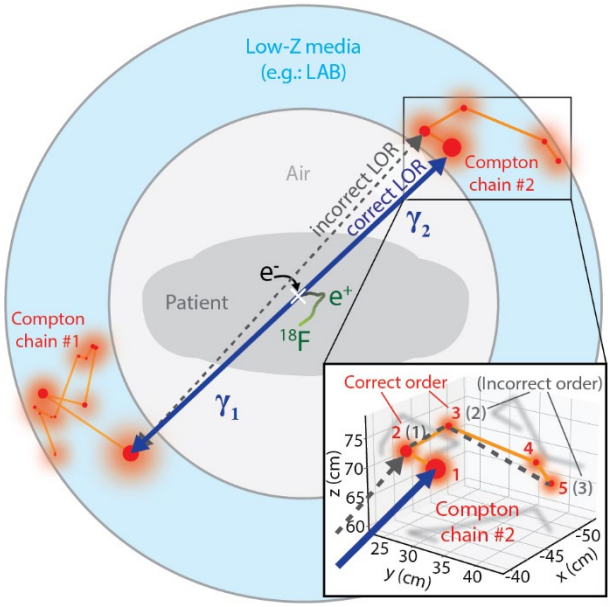

Fig. 1. Schematic of proposed TOF-PET detection scheme using first Compton scatter location to determine a line of response (LOR). Low-Z detection media such as linear alkylbenzene (LAB) containing a switchable reporter such as a photoswitchable fluorophore surrounds the patient. A positron (green e^+) originating from the decay of a radiotracer (here: ^{18}F) diffuses (green track) and annihilates with an electron (black e^-, white x). Each of the two resulting back-to-back gamma photons (dark blue) interacts with the LAB via a chain of Compton scattering events (red/orange; circle area is proportional to recoil electron energy). The correct line-of-response (LOR) connects the first Compton scatter of each chain; mis-identification of the first interaction will result in an incorrect LOR (gray dashed line). *Inset:* Different possible orderings of Compton scatters in one simulated chain (shadows show 2-D projections) are proposed and selected using a likelihood-based figure of merit (FOM); here one incorrect ordering is shown (gray dashed line; FOM = 20.88) along with the true ordering (orange / blue; FOM = 0.922).

III. METHODS

A. TOPAS Simulation of TOF-PET and Data Validation

We constructed and parameterized a simulation of a whole-body TOF-PET scanner using TOPAS 3.8 [37] running the Geant4 physics modules "g4em-standard opt4" and "g4em-penelope" [38]–[42]. The cylindrical detector (2 m long; bore diameter 90 cm; radial thickness 30 cm) is filled with high purity LAB (density 0.860 g/cm^3, composition 87.86% H, 12.14% C [43]; mean excitation energy 59.4 eV [44]), with an air core. Intrinsic radioactivity of detector media is expected to be negligible and is not simulated.

Different ^{18}F imaging sources can be positioned within the bore of the detector; in this work we used the Derenzo geometric phantom [45], the XCAT human phantom [46], and a positron point source. The per volume activity for each phantom is benchmarked to typical activity in a patient with a "standard dose", calculated as 5 MBq/kg and a baseline imaging time of 10 minutes. All simulations in this work were performed with a reduced dose, set at or below 1/100 of the standard dose. Simulations include in-patient scattering.

TOPAS generates a set of ^{18}F positrons throughout the source volumes, which are passed to Geant4 for propagation. Geant4 handles positron diffusion and annihilation, generating pairs of gamma photons that propagate through the simulation volume. We wrote a custom C++ scoring extension for TOPAS to records events in the detector volume. The minimum step size was set to 10 μm. Simulations were run on a 14-thread processor (Intel Xeon CPU E5-2620v4 at 2.10 GHz), with runtimes between 15 and 70 hours for 83 million positrons, depending on the complexity of the phantom geometry. Ground truth output data include times and Cartesian positions of interactions, the energy balance of each interaction, and all particle identities. All custom code and supporting documentation are available for download online [47].

We validated our simulation by comparing its output with well-established physical phenomena. Fig. 2a and 2b show the simulated distributions of drift distance and kinetic energy, respectively, of positrons at annihilation. The distributions agree well with published results: the full width half maximum of the positron drift distance is 0.347 mm, and the majority (98.4%) of positrons have identically zero kinetic energy upon annihilation [48]–[50]. Fig. 2c shows the distribution of initial distances traveled into LAB by gamma photons prior to interaction, as well as the distance between the first and second scatters in LAB. The simulated initial distance corresponds well to the calculated 1/*e* stopping distance of LAB (12.05 cm) [31].

The scattering angles and the outgoing energies in each scatter are constrained by the electron-gamma photon two-body kinematics (assuming free electrons). Fig. 2d shows the event-by-event relationship between the simulated scattering angle and the recoil electron energy for primary 511 keV gamma photons. The Compton formula (dotted blue) fits the simulated data well. The inset shows a profile at a scattering angle of $\pi/4$. The profile width is due to modeling of electron binding and kinetic energy by the Penelope package [51], and has a two-tailed exponential spread with a decay constant of 2.04 keV^{-1}, matching the expected value for carbon [52].

The ground truth simulation results also benchmark the expected behavior of a low-Z TOF-PET detector: Fig. 2e shows the distribution of the number of scatters observed in Compton chains within the detector, averaging 10.1 scatters per chain and heavily skewed towards a lower number of scatters. Fig. 2f shows the fraction of all Compton scattering events at each recoil electron energy *E*. As expected, the

recoil electron energy trends downward with successive scatters, and the first scatter distribution is well-fit by the Klein-Nishina model (dotted black) [53].

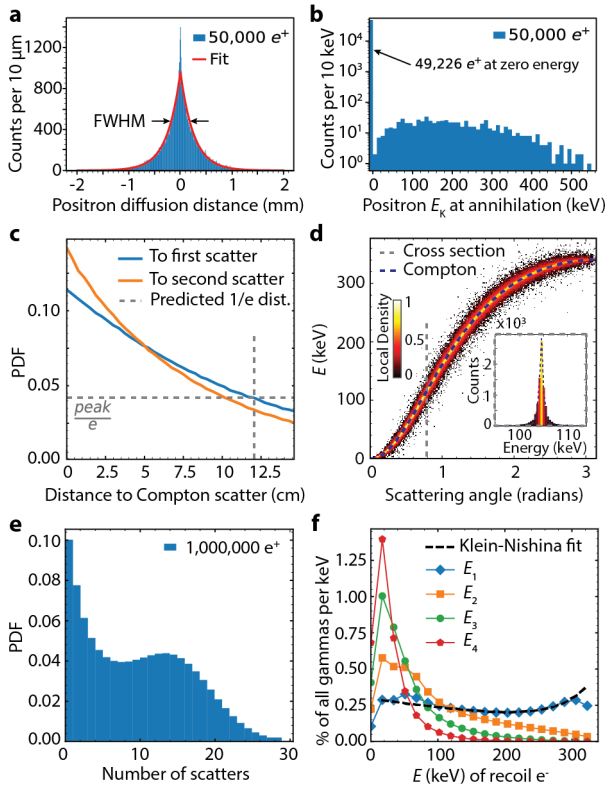

Fig. 2. Simulation validation and characterization. a) Histogram of positron diffusion distance prior to annihilation (blue) and fit (red), with FWHM 0.347 mm. b) Histogram of positron kinetic energy at annihilation (blue) is mostly identically 0 keV (98.4%). C) Gamma distance into the LAB medium before first Compton scattering event (blue) and distance between first and second Compton scattering events (orange). The expected 1/*e* range for LAB (12.05 cm) is shown in gray dashed crosshairs. d) 2-D histogram of energy deposited in the first Compton scattering event (*E*, red-yellow heatmap) for each scattering angle, closely matches the theoretical prediction from the Compton relation (dotted blue). Inset: Cross-section at $\theta = \pi/4$, with double-sided exponential fit (dotted blue). E) Histogram of the number of Compton scattering events observed in each chain. f) Histograms of energy deposited in the first (blue / diamond), second (orange / square), third (green / circle) and fourth (red / pentagon) Compton scatters in a chain, respectively. A fit to the Klein-Nishina cross section is shown as a black dashed line.

B. Simulation of Detector Resolution

To simulate detector measurements and study how system performance depends on detector parameters, random noise was applied to the ground truth simulation data according to the detector's energy, timing, and spatial resolution parameters. Error in energy measurements arises from uncertainty in the extent of the recoil electron's effect on the detection medium. All added noise was Gaussian-sampled. Assuming a two-state molecular recorder, the efficiency k_E with which the recoil e^- of energy *E* produces switched molecules, $N(E) = E/k_E$ (units keV/switch), determines the back-propagated uncertainty in electron energy, σ_E, using the uncertainty of counting *N* switched molecules, $\sqrt{N}$, according to

$$\sigma_E(E) = k_E\sqrt{N(E)} = \sqrt{k_E \cdot E} \quad (1)$$

where $N(E)$ is rounded to the nearest integer. If the resulting noise-corrupted E happens to be negative (possible for small $N(E)$ events), the event is discarded. Spatial uncertainty, σ_x, is directly applied to ground truth scattering locations. Timing uncertainty, $\mathrm{FWHM_t}$, is directly applied to ground truth interaction times. For the purposes of the following analyses we ignore pile-up; we assume that the records corresponding to each chain of Compton scatters can be correctly grouped. This might be experimentally achieved, for example, using coincidence timing of initial light from each scatter.

The default resolutions for simulation are set as follows: The energy resolution is set by k_E with a default value of 1 keV/switch. The default spatial resolution of scattering locations, σ_x, is a 1 mm standard deviation. The default timing resolution, $\mathrm{FWHM_t}$, is conservatively set to 500 ps. Variation of these parameters is studied in *IV.C. Effect of Tuning Detector Parameters*.

C. Statistical Determination of Lines-of-Response

Simulated detector data are used to reconstruct TOF-PET images based upon the aggregate information from many individual lines of response (LORs). For low-Z detection, the line of response for each annihilation event is drawn between the first Compton scattering location for the back-to-back gamma photons. Image reconstruction therefore first requires correct ordering of each Compton chain. While the detector may also provide timing information using scintillation or Cherenkov light, it is not strictly necessary; here we develop an ordering algorithm based solely on the geometry and energy of scattering interactions.

We developed an algorithm to determine the most probable ordering (and therefore first scatters) in each pair of Compton chains using the overall geometry and measured energies of each set of scatters. For each individual event i causing an apparent change in trajectory, θ_i, of a gamma photon and producing a recoil electron with energy E_i, the expected incoming gamma photon energy, $E_{\gamma i}^{\mathrm{Comp}}$, is given by

$$E_{\gamma i}^{\mathrm{Comp}} = \frac{E_i + \sqrt{E_i^2 + \frac{4E_i m_e}{1-\cos\theta_i}}}{2} \tag{2}$$

where m_e is the rest mass of the electron.

An alternative estimate of the incoming gamma photon energy, $E_{\gamma i}^{\mathrm{chain}}$, can be calculated based on the preceding series of recoil electron energies E_j, along with the initial gamma photon energy of 511 keV:

$$E_{\gamma i}^{\mathrm{chain}} = 511\ \mathrm{keV} - \sum_{j=1}^{i-1} E_j \tag{3}$$

where E_j is the observed energy at scatter j.

Propagation of error gives the uncertainty in each estimate of $E_{\gamma i}$ as calculated using $k_E(E)$ and the uncertainty in angular redirection, $\sigma_\theta(\vec{x}_{i-1}, \vec{x}_i, \vec{x}_{i+1}, \sigma_x)$, which is calculated from scatter locations and the spatial uncertainty σ_x. Given these uncertainties, we generate a figure of merit for each individual scatter in a proposed chain order, $\mathrm{FOM_i}$, using a two-tailed Z-score:

$$\mathrm{FOM}_i = \frac{\left|E_{\gamma i}^{\mathrm{chain}} - E_{\gamma i}^{\mathrm{Comp}}\right|}{\sqrt{\left(\delta E_{\gamma i}^{\mathrm{chain}}\right)^2 + \left(\delta E_{\gamma i}^{\mathrm{Comp}}\right)^2}} \tag{4}$$

where $\delta E_{\gamma i}^{\mathrm{chain}}$ is the uncertainty in $E_{\gamma i}^{\mathrm{chain}}$, and $\delta E_{\gamma i}^{\mathrm{Comp}}$ is the uncertainty in $E_{\gamma i}^{\mathrm{Comp}}$.

Possible chain orders are tested in a recursive tree search, keeping only the current minimum FOM solution and terminating search branches above a threshold set to a chain length-adaptive value of 1.3 FOM per scatter. Unpaired chains where only one gamma photon created a detector interaction are discarded. Pairs of chains where one or both gamma photons undergo significant in-patient scattering fail the FOM test.

D. Image Reconstruction

The LOR defined by locations and timing of each pair of first scatters is a needle-shaped 3-D Gaussian probability density describing the location of each annihilation. A TOF-PET image can be reconstructed based on the collective spatial distribution of all LORs. Filtered back-projection (FBP) and other common TOF-PET reconstruction algorithms are designed for discretized LORs and traditional detectors. Here, LOR positions and orientations for a low-Z detector are continuous; a sophisticated reconstruction algorithm using appropriate weights would require a fully characterized active medium, a realistic optical design, and would take full advantage of the correlated spatial and temporal data. Therefore, in this work we reconstruct images by summation of probabilities for all LORs over a voxelized volume slice (22 cm x 22 cm x 0.5 mm with 0.125 mm^3 cubic voxels). Each image is normalized by the integrated transverse profile of the LOR. All reconstructed image slices shown in this work are taken perpendicular to the detector axis, centered on the origin.

E. Sensitivity, Spatial Resolution, and Contrast-to-Noise (CNR) Criteria

Two fundamental criteria for evaluating TOF-PET performance are its efficiency in detecting emitted gamma photons, or *sensitivity*, and the width of its point spread function, or *spatial resolution*. Here, we calculate sensitivity, *S*, directly from simulated data of a point source in vacuum placed at the origin, using the ground truth number of pairs of gamma photons that interact with the detector, n_{pair}, compared to the total number of positrons simulated, $N_{e+} = 10^6$ positrons, according to

$$S = \frac{n_{pair}}{N_{e+}} \tag{5}$$

This criterion is based on the NEMA NU-2018 definition of TOF-PET sensitivity [54], substituting a point source for the line source so that the same simulated data can be used to calculate the PSF. The full width at half maximum (FWHM) and full width at tenth maximum (FWTM) of a transverse image slice through the reconstruction of this PSF define the spatial resolution per the NEMA NU-2018 criteria [54].

To evaluate the fidelity and quality with which reconstructed images represent the true radiotracer distribution within the subject, we also calculate the contrast-to-noise ratio (CNR) for well-established features of certain phantoms according to

$$CNR = \frac{\bar{p}_1 - \bar{p}_0}{\sigma_{p0}} \tag{6}$$

where $\bar{p}_1$ is the average value of pixels in the signal region, $\bar{p}_0$ is the average value of pixels in the background region, and σ_{p0} is the standard deviation of pixels in the background region. Image regions are masked according to the known geometry of the phantom. Rod CNRs are averaged by size group. See the *Appendix I* for mask details and rod-by-rod CNR analysis.

F. LYSO Simulation

For the benchmarking simulation using crystalline lutetium-yttrium oxyorthosilicate (LYSO) as the detection medium, the thickness of the detection volume is reduced to 15 cm, and standard LYSO material parameters are used (density 7.40 g/cm^3, composition 71.4468% Lu, 4.0338% Y, 6.3714% Si, 18.148% O; mean excitation energy 411 eV) [55]. The detector volume is modeled as continuous, and for the purposes of simulating the detected position, the ground truth interaction position is randomized by a flat distribution the size of the 3mm x 3mm x 10mm crystal. The crystals are oriented with the long axis facing radially. Note that the LORs for LYSO are only Gaussian in their longitudinal direction due to TOF; their transverse probability profiles are flat due to the segmented crystal geometry. For simplicity, we used a 3mm diameter circular cross section for all LORs (no parallax). Timing uncertainty $FWHM_t$ = 300ps is applied directly to ground truth. Energy resolution based on a yield of 30,000 photons/MeV for LYSO was applied [56]. An energy threshold of within 25% of 511 keV was applied to events to reject in-patient-scatters.

IV. RESULTS

A. Comparison of Low-Z to State-of-the-Art TOF-PET

We benchmarked the default simulation parameters for a low-Z LAB detector (k_E = 1 keV/switch, σ_x = 1 mm, $FWHM_t$ = 500 ps) against a state-of-the-art lutetium-yttrium oxyorthosilicate (LYSO) crystal detector (crystal size of 3mm x 3mm x 10mm), both simulated as described in *III. Methods*. The thinner LYSO detection volume (15 cm vs. 30 cm for LAB) is comparable to state-of-the-art instruments [24]. For a point source in vacuum, the sensitivity of the LAB detector is 70% (6.998 x 10^6 LOR / 10^7 positrons). The sensitivity of the LYSO detector is 12.4% (1.244 x 10^6 LOR / 10^7 positrons), in rough agreement with the experimental values reported for a similar instrument with slightly higher angular coverage, the uEXPLORER whole-body TOF-PET scanner [24].

Fig. 3a and 3b show reconstructed images of a water-filled Derenzo phantom at 1/100 standard dose (rods: 150 Bq/ml; background: 50 Bq/ml) located at the origin with rods parallel to the detector axis, simulated for LAB and LYSO detectors, respectively. Note that for the LYSO image in Fig. 3b, the display contrast is enhanced 6x to facilitate comparison with Fig. 3a, as reflected by their respective colorbars. The LAB image appears brighter, sharper, and less noisy, which may be partially attributed to the higher sensitivity and therefore the higher number of LORs used in the image.

We compared the PSFs of the LAB and LYSO detectors using a point source in vacuum. The PSF profiles are shown in Fig. 3c. The LAB spatial resolution is slightly better (FWHM = 4.6 mm) than the LYSO (FWHM = 5.3 mm), but both are comparable. These resolutions would be improved substantially by a more sophisticated image reconstruction algorithm, and here serve only to illustrate that a moderate estimate of a low-Z detector's Compton localization precision performs as well as or better than the current state-of-the-art.

As shown in Fig. 3d, the LAB scanner produces better contrast-to-noise ratios for all but the largest rod size in the Derenzo phantom. These differences are more pronounced for smaller rods (65%, 50% for the 6.4 mm and 7.5 mm rods, respectively). The near identical values for the largest rod may be due to systematic effects on the noise measurement; see Appendix . If the rod has a smooth transition towards

the peak value a measurement of the noise will be dominated by the curvature rather than random fluctuations. As the rods get larger they get closer to this smooth behavior, leading to a more heavily systematically dominated CNR. Rejection of in-phantom scatters by the FOM Compton chain ordering algorithm (8.3% of LORs are in-patient scatters) performs well; for comparison, a ±25% energy-based cutoff for the LYSO detector has 22.5% of LORs are in-phantom scatters.

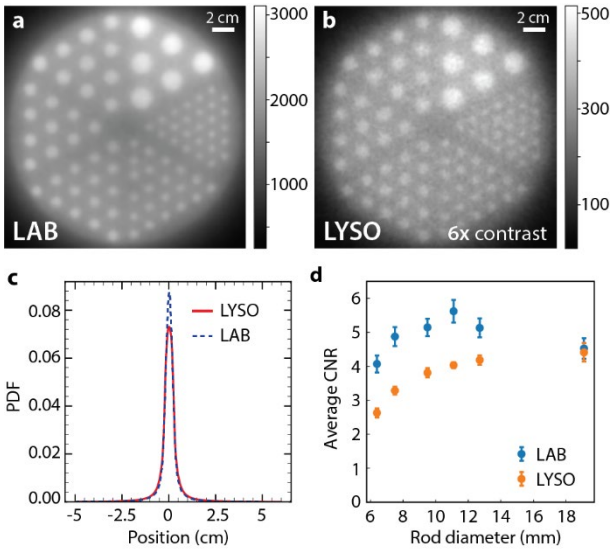

Fig. 3. Comparison of the proposed method to current advanced TOF-PET detection. a) Reconstructed image of a Derenzo phantom for a low-Z LAB detector, at 1/100 of standard dose, reconstructed from 3.55 x 10^6 LORs. b) Reconstructed image of a Derenzo phantom for an LYSO crystal detector, at 1/100 of standard dose, reconstructed from 6.58 x 10^6 LORs, shown at 6x contrast as compared to panel *3a* due to lower sensitivity. c) PSF of LAB and LYSO simulations, acquired by simulating a point source in vacuum. FWHM of the LYSO PSFs is 5.3 mm; FWHM for LAB is 4.6 mm. d) Mean contrast-to-noise ratio (CNR) of LAB and LYSO simulations for rod sizes represented in the Derenzo phantom.

B. Sources of error in Low-Z TOF-PET imaging

Because a low-Z detection approach requires likelihood-based ordering of a Compton scattering chain, in which events can be separated by many centimeters, mis-identified first scatters can cause LOR and reconstruction errors that would not be present in standard TOF-PET. If both Compton chains are correctly reconstructed, the LOR is definitionally correct. An image reconstructed from the set of all such correct LORs (2.503 x 10^7 LORs) for a Derenzo at 1/100 dose is shown in Fig. 4a, and appears slightly sharper and cleaner than Fig. 3a.

If instead one or both chains have an incorrect first scatter, the LOR will be incorrect (1.046 x 10^7 LORs). Fig. 4b shows the Derenzo reconstructed from all incorrect LORs. Surprisingly, this image is still recognizable as a Derenzo phantom, indicating that some incorrect LORs still contain valuable information. Indeed, a distribution of the miss distance for all incorrect LORs, shown in Fig. 4c, is bimodal. Incorrect LORs that miss the true annihilation location by several centimeters are a result of general failures of the chain ordering algorithm as expected. The second population, which we term “near miss”, falls within 2 mm of the correct location of annihilation. Of the total 70% sensitivity for the LAB detector, 61.4% are correct LORs, 4.35% are near-misses, and 4.25% are incorrect.

We found that the near-miss LORs tend to arise for Compton chains with one of two specific features. The first is a very low energy first scatter (10 keV or less) followed by a larger second scatter. Due to the very small first scatter, the second scatter tends to be close to the original trajectory, and therefore produces a near-miss LOR if it is mis-identified as first. Alternatively, if any scatter that is mis-identified as first is sufficiently close to the true first scatter, the LOR will be a near miss. Such close proximity of another scatter to the first scatter limits the discriminative power of the ordering algorithm, but without a meaningful loss in fidelity.

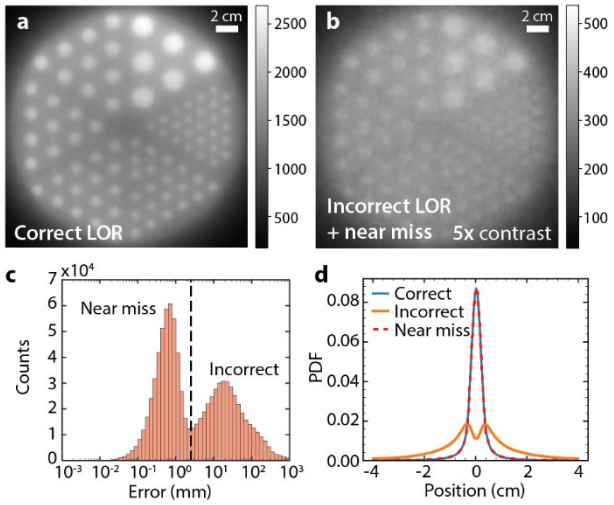

Fig. 4. Effect of incorrect Compton chain ordering on reconstructed image and LORs. a) Image reconstructed from only Compton chains that resulted in a correct order and therefore correct LOR (2.50 x 10^7 LORs). b) Image reconstructed from all Compton chains that did not result in correct ordering, shown at 5x enhanced contrast as compared to 3a) (1.05 x 10^7 LORs). c) Histogram of error between all incorrect LORs and ground truth for a point source, divided into two populations "near miss" and "incorrect" according to the magnitude of error (dashed line set at 2 mm). d) PSFs of correct LOR as compared to near misses and incorrect LOR for a point source. FWHM of correct and near miss LOR is 4.6 mm. experimental values reported for a similar instrument with slightly higher angular coverage, the uEXPLORER whole-body TOF-PET scanner [24].

C. Effect of Tuning Detector Parameters

To place upper and lower bounds on the technical requirements and to better understand the potential advantages and limitations of low-Z detectors for advanced TOF-PET, we simulated a range of detector resolution parameters, including energy resolution, spatial resolution, and temporal resolution. Other parameters were held at their default values. All parameters were applied as described in *III. Methods*. For each parameter, we determined the effect on i) image spatial resolution as measured by the FWHM and FWTM of the PSF for a point source, ii) detector sensitivity, including a breakdown of correct, incorrect, and near-miss LOR percentages, and iii) the average CNR for rods in the Derenzo phantom at 1/100 dose. For each set of parameters, we also display the best Derenzo image.

Energy resolution is controlled by k_E, the efficiency of switching (keV per switch). We tested k_E values of 1, 5, 10, 50, and 100 keV/switch (default: 1 keV/switch). Fig. 5a-c show the effect of energy resolution on the image spatial resolution, the detector sensitivity, and the CNR for Derenzo rods. Changes in k_E do

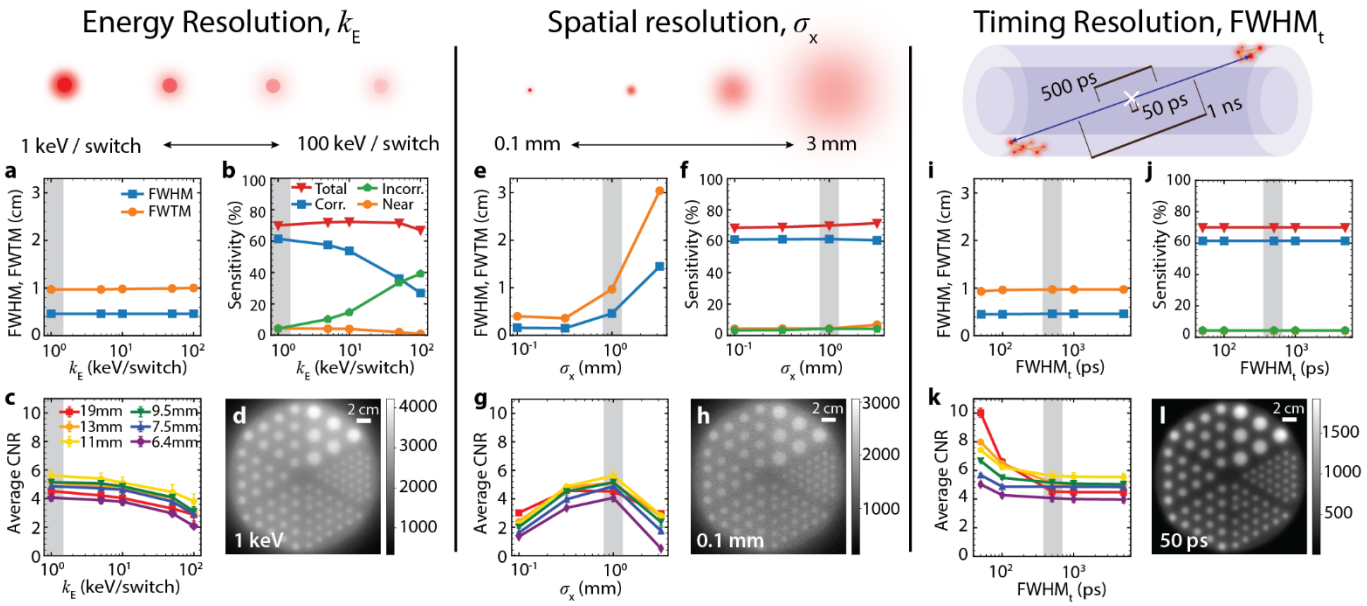

Fig. 5. Effect of energy resolution, spatial resolution, and timing resolution on TOF-PET resolution, sensitivity, contrast-to-noise ratio, and image quality. Gray highlights indicate baseline parameters: kE = 1 keV/switch, σx = 1 mm, FWHMt = 500 ps. All Derenzo phantoms were run at 1/100 of a standard dose. a) FWHM (blue) and FWTM (orange) of PSF for varying kE. b) Sensitivity for varying kE, shown as total sensitivity (red / triangles), correct LORs (blue / squares), incorrect LORs (green / pentagons), and near-miss LORs (orange / circles). c) CNR for varying kE across different dot sizes for the Derenzo phantom. d) Highest-quality image for varying kE is obtained at kE = 1 keV/switch, at fixed σx = 1 mm and FWHMt = 500 ps. e) FWHM (blue) and FWTM (orange) of PSF for varying σx. f) Sensitivity for varying σx, shown as total sensitivity (red / triangles), correct LORs (blue / squares), incorrect LORs (green / pentagons), and near-miss LORs (orange / circles). g) CNR for varying σx across different dot sizes for the Derenzo phantom. h) Highest-quality image for varying σx is obtained at σx = 0.1 mm, at fixed kE = 1 keV/switch and FWHMt = 500 ps. i) FWHM (blue) and FWTM (orange) of PSF for varying FWHMt. j) Sensitivity for varying FWHMt, shown as total sensitivity (red / triangles), correct LORs (blue / squares), incorrect LORs (green / pentagons), and near-miss LORs (orange / circles). k) CNR for varying FWHMt across different dot sizes for the Derenzo phantom. l) Highest-quality image for varying FWHMt is obtained at FWHMt = 50 ps, at fixed kE = 1 keV/switch and σx = 1 mm.

not lead to a substantial change in image spatial resolution (Fig. 5a), but decreasing energy resolution (higher k_E) leads to substantial losses in detector sensitivity, with many scatters no longer being correctly identified (Fig. 5b). The decreasing sensitivity also causes loss of CNR in the Derenzo phantom shown in Fig. 5c. The best Derenzo image, shown in Fig. 5d, results from the best energy resolution (1 keV/switch).

We tested scatter localization spatial resolutions, σ_x, of 0.1, 0.32, 1.0, and 3.2 mm (default: 1 mm). Fig. 5e-g show the effect of σ_x on the image spatial resolution, the detector sensitivity, and the CNR for Derenzo rods. Smaller σ_x directly improves image spatial resolution (Fig. 5e), but does not affect detector sensitivity (Fig. 5f) as the tested spatial resolutions are still small compared to typical distances between scatters. The measured CNR increases for smaller σ_x as expected; the drop below 1 mm can be attributed to insufficient voxel sampling (Fig. 5g). The best Derenzo image, shown in Fig. 5h, results from the best σ_x (0.1 mm).

We tested timing resolutions, FWHM$_t$, of 50, 100, 500, 1000, and 5000 ps (default: 500 ps). Time resolution has little effect on the image spatial resolution of a point source because even the best timing resolutions translate to large spatial uncertainties compared to σ_x, as shown in Fig. 5i. Changing the time

resolution has no effect on the detector sensitivity, as our Compton reconstruction algorithm does not currently use timing information, as shown in Fig. 5j. Timing does strongly affect CNR, as shown in Fig. 5k, with improved timing removing pileup of LORs outside of their origin location. This helps to remove a blurred background. The best Derenzo image, shown in Fig. 5l, results from the best $FWHM_t$ (50 ps).

D. Ultra-Low-Dose TOF-PET via Low-Z Detection

Potential clinical applications of the low-Z scanner were investigated by running simulations on a human phantom. Using our baseline detector parameters of k_E = 1 keV/switch, σ_x = 1 mm, $FWHM_t$ = 500 ps, we were able to generate clear images of the brain at ultra-low doses. The brain phantom is created using 4D Extended Cardiac-Torso (XCAT) phantom software, which produces voxelized patient geometries that can easily be simulated in TOPAS. Our phantom had no anatomical abnormalities. Densities and atomic compositions of the tissues were modeled using data from the International Commission on Radiological Protection (ICRP) [57], [58] and the International Commission on Radiation Units and Measurements (ICRU) [59]. Based on tissue-specific uptake ratios [60] and the standard dose as defined in *III. Methods*, we calculated the standard radiotracer dose in the brain to be 33 kBq/mL in the gray matter and 8.25 kBq/mL in the white matter. We imaged the brain phantom in the presence of the full XCAT body phantom. Simulations were run both without and with an added 20 mm diameter spherical lesion (99 kBq/mL) following Lee and co-workers [61].

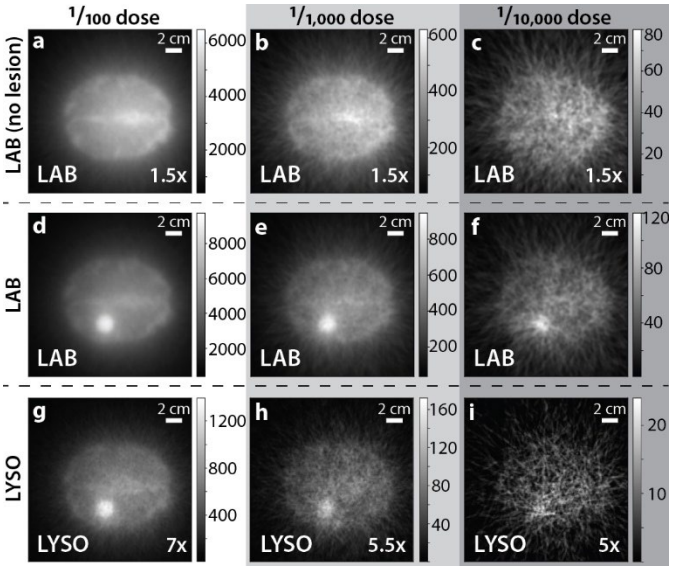

Fig. 6. Low-dose brain imaging, axial view. a)-c) Reconstructed images of the XCAT brain simulated using 1/100, 1/1000, and 1/10000 dose of 18F and LAB detection medium, respectively; each is shown at 1.5x contrast compared to the corresponding dose / image for d-f. d)-f) Reconstructed images of the XCAT brain + lesion, simulated using 1/100, 1/1000, and 1/10,000 dose of 18F and LAB detection medium, respectively. g)-i) Reconstructed images of the XCAT brain + lesion simulated using 1/100, 1/1000, and 1/10,000 dose of 18F and LYSO crystals for detection, respectively; shown at 7x, 5.5x, and 5x contrast compared to the corresponding doses / images for d-f. Standard full-dose activity for white matter is taken to be 8.25 kBq/mL, gray matter is 33 kBq/mL, and the lesion is 99 kBq/mL; standard scan duration 10 min.

In Fig. 6, we present images of the brain at 1/100th, 1/1,000th, and 1/10,000th doses using both the low-Z LAB detector and the LYSO detector described above. At 1/100th dose, both the detectors perform well, clearly showing the tumor, gray matter, and white matter, but the LAB image has the

benefit of being seven times brighter due to its higher sensitivity. At 1/1,000th dose, both detectors can identify the tumor, but in the LAB image gray and white matter can still be distinguished. At 1/10,000th dose, the tumor is still readily apparent against the gray and white matter in the LAB detector, but it is much harder to spot for the LYSO detector.

V. DISCUSSION

Here we have taken advantage of the TOPAS simulation framework for Geant4 to write a parametric simulation of a full-body TOF-PET detector based on an ionization-sensitive low-Z persistent recording medium and fast MCP-based photodetectors to record the chain of Compton scattering from annihilation gamma photons. The TOPAS framework facilitates high fidelity physics simulations that separate the detector design from the underlying physics, so that detector variants and interchangeable phantoms can be easily tested.

Using these simulations, we benchmarked the predicted performance of a low-Z detector-based TOF-PET instrument as previously proposed [26]. In comparison to traditional scintillation-crystal based TOF-PET detectors, a low-Z detector is predicted to have more than 5x higher sensitivity, comparable or better spatial resolution, and 40-50% better contrast to noise in reconstructed images. We also showed that such a detector could be used for ultra-low-dose brain imaging at 1% or even 0.1% of a standard radiotracer dose.

Many of the advantages our results predict for a low-Z TOF-PET detector stem from enhanced sensitivity. Given our detector geometry, the theoretical maximum sensitivity is 73%, so the 70% sensitivity predicted for the low-Z simulations in this work is nearly optimal. Since low-Z detection media are cheap relative to scintillation crystals, implementation of low-Z detectors with high stopping power is reasonably realistic. The improvements to sensitivity relative to LYSO are primarily due to the abundance of relevant interactions: Scintillating crystal detectors screen for photoelectric interactions, yet the LYSO Compton cross-section is twice as large as its photoelectric cross section [31].

The simulations presented in this work do not account for several factors that would influence design and efficacy of a real-world low-Z detector. For example, we assume that Compton scatters can be assigned to the correct chain, and that pairs of chains are correctly identified. Our simulations also do not account for any aspect of timing methodology; here shorter scan durations and lower radiotracer doses are treated as interchangeable, but these distinctions will become critical in the context of detection hardware and design choices. For example, here possible pile-up effects are not considered because the wide-field readout technology is not modeled, but we note that the combination of a large detection volume with precise timing provides a range of options for event separation as well as excitation and reset light patterning.

The approach described here could be further enhanced by using full timing and spatial information, including scintillation flashes, distances between scatters, and the planes of scattering and gamma polarization effects; note that in this work only recoil electron energies E and scattering angles were considered. If the directional tracks of the recoil electrons can be visualized in addition to their general location, the scattering locations could be determined much more precisely, and the recoil electron's initial trajectory could be included in the ordering algorithm. It might also be possible to infer the locations of in-patient scattering so that these detection events can also be used for image reconstruction. For this

information-rich system, determination of scattering locations and timing, most probable LORs, and image reconstruction are all likely to be fertile ground for machine learning.

Without a sophisticated reconstruction algorithm, the predicted resolutions reported here are expected to underestimate the resolution performance of a fully developed system. This is apparent in the simulated resolution of an LYSO system, as compared to state-of-the-art reconstruction algorithms that produce a nearly twofold enhanced spatial resolution in real-world instruments [24]. Additional effects including parallax and a parallelogram-shaped LOR for scintillating crystals were not considered here. Direct reconstruction without filtered back-projection also leaves a $1/r^2$ falloff on all edges, limiting image sharpness. Nonetheless, a qualitative comparison of image resolution using this algorithm indicates that a low-Z detector could perform comparably or better than a scintillating crystal. We expect that low-Z detector resolution could rapidly approach positron diffusion limits of tenths of a mm since scatter location should be readily measurable to a high degree of precision, particularly if any information about the recoil electron's trajectory is available.

Future prospects for this detection technique depend on development of an appropriate persistent low-Z medium to record Compton scatters. Among candidates, photo-switchable dyes in solution with a fast scintillator and energy-transfer-enhancing mediators, or another switchable two-state molecular system, may be desirable [46]. A similar low-Z detection approach could be implemented for single photon emission computed tomography (SPECT) detection applications.

VI. CONCLUSION

Ultra-low dose TOF-PET would profoundly impact both preclinical and clinical applications. For existing applications, higher sensitivity and resolution would allow smaller features to be identified, such as early-stage tumor metastases, improving healthcare outcomes. Lowered radiation doses would be appropriate for a wider range of patients, including pediatric and pregnant populations. More PET scans could be performed for the same radioactive exposure, allowing more frequent and widespread use, for example for medical screening. Lower doses could also expand geographic access to TOF-PET. At 1/100 dose the radiotracer viability window could be extended by up to 6.5 half-lives; at 1/1000 dose it could be extended by as much as 10 half-lives, relaxing the required proximity to a cyclotron and other infrastructure.

Taken together, the simulations reported here illustrate the potential benefits and limitations of a low-Z TOF-PET detector, and show that reasonable technical specifications (1 keV / switch for energy resolution, 1 mm resolution of scatter location, and 500 ps FWHM timing resolution) would enable high-quality TOF-PET imaging with significantly reduced radiotracer doses.

ACKNOWLEDGEMENT

For their exemplary software development and user support, we thank both Joseph Perl (TOPAS) and Paul Segars (XCAT). We thank Mary Heintz for essential computational system support. For financial support of undergraduate research from University of Chicago College, Physical Sciences Division, and Enrico Fermi Institute, we thank Steven Balla and Nichole Fazio, Michael Grosse, and Scott Wakely, respectively. We also thank the participants and organizers of the DOE / NIH workshop "Advancing

Medical Care through Discovery in the Physical Sciences: Radiation Detection" (Jefferson Lab, April 2023) for their helpful discussions and feedback.

APPENDIX: CONTRAST-TO-NOISE RATIO (CNR)

This appendix provides additional details of the CNR calculations performed for the Derenzo phantom. Fig. 7a shows the rod numbering scheme referred to throughout this Appendix. Rods are numbered from largest to smallest, inside to outside. Fig. 7b and 7c show the signal and background masks, respectively, applied here to a reconstructed image from the benchmark low-Z simulation.

Based on the data from these masked regions and from Fig. 3a, there are apparent spatial biases in the resulting CNR calculations, as illustrated by Fig. 7d-f. The outer rods have significantly lower CNR values because the outer edges of their background regions are generally darker than rod backgrounds closer to the middle of the image, which makes for both higher contrast (Fig. 7d) and higher noise (Fig. 7e). However, the difference in the noise between these outer rods and the others is greater than differences in contrast, which creates a lower overall CNR value. This is because low spatial frequency brightness changes dominate the noise, with the background gradually lightening as it moves from the outer edge of the phantom toward the center, which occurs due to the direct image reconstruction approach which creates $1/r^2$ falloff.

Systematic spatial variations are also responsible for the drop in average CNR values for the largest rod size as shown in Fig. 3d. Fig. 7c reveals that the background around the largest rods also exhibit the $1/r^2$ effect near the rod edges, appearing dimmer in between. This effect is most pronounced for the largest rods, where the spacing is also largest, inflating the standard deviation and lowering the CNR.

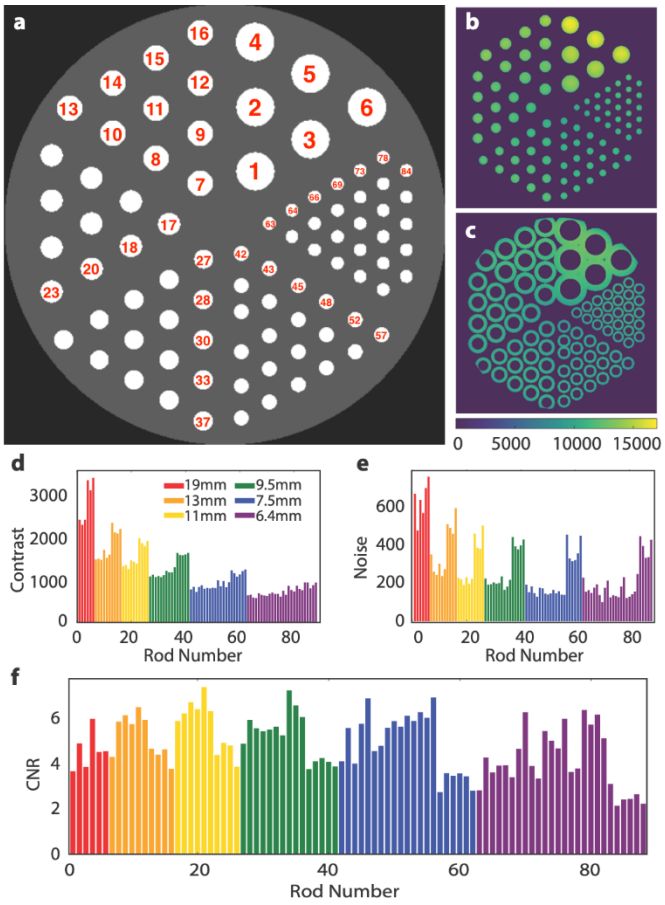

Fig. 7. CNR masks and individual rod CNR values for the Derenzo phantom. All panels refer to the simulation for LAB with baseline parameters. a) The numbering scheme for the rods as later represented in d-f. b) The mask used to determine signal of each rod, covering the entire diameter of the rod as given by the truth information. c) A mask depicting the areas used to calculate noise of each rod, covering a ring from 1.2 to 1.9 times the radius of the rod, but excluding anything within ten pixels of the phantom's true edge. d) Contrast values for each rod, calculated by subtracting the average brightness of the background ring from the average brightness of the rod. e) Noise values for each rod, calculated with the standard deviation of the brightness of each background ring. f) CNR for each rod, calculated by dividing the contrast by the noise per Eqn. 6 in the main text.

REFERENCES

[1] S. R. Cherry, R. D. Badawi, J. S. Karp, W. W. Moses, P. Price, and T. Jones, "Total-body imaging: Transforming the role of positron emission tomography," Sci. Transl. Med., vol. 9, no. 381, p. eaaf6169, Mar. 2017, doi: 10.1126/scitranslmed.aaf6169.

[2] M. Conti and B. Bendriem, "The new opportunities for high time resolution clinical TOF PET," Clin Transl Imaging, vol. 7, no. 2, pp. 139–147, Apr. 2019, doi: 10.1007/s40336-019-00316-5.

[3] S. Surti and J. S. Karp, "Update on latest advances in time-of-flight PET," Physica Medica, vol. 80, pp. 251–258, Dec. 2020, doi: 10.1016/j.ejmp.2020.10.031.

[4] W. W. Moses, "Fundamental limits of spatial resolution in PET," Nuclear Instruments and Methods in Physics Research Section A: Accelerators, Spectrometers, Detectors and Associated Equipment, vol. 648, pp. S236–S240, Aug. 2011, doi: 10.1016/j.nima.2010.11.092.

[5] S. R. Cherry, "The 2006 Henry N. Wagner Lecture: Of mice and men (and positrons)--advances in PET imaging technology," J Nucl Med, vol. 47, no. 11, pp. 1735–1745, Nov. 2006.

[6] W. W. Moses, "Recent advances and future advances in time-of-flight PET," Nuclear Instruments and Methods in Physics Research Section A: Accelerators, Spectrometers, Detectors and Associated Equipment, vol. 580, no. 2, pp. 919–924, Oct. 2007, doi: 10.1016/j.nima.2007.06.038.

[7] S. Surti, "Update on Time-of-Flight PET Imaging," J Nucl Med, vol. 56, no. 1, pp. 98–105, Jan. 2015, doi: 10.2967/jnumed.114.145029.

[8] J. J. Vaquero and P. Kinahan, "Positron Emission Tomography: Current Challenges and Opportunities for Technological Advances in Clinical and Preclinical Imaging Systems," Annu. Rev. Biomed. Eng., vol. 17, no. 1, pp. 385–414, Dec. 2015, doi: 10.1146/annurev-bioeng-071114-040723.

[9] S. Vandenberghe, P. Moskal, and J. S. Karp, "State of the art in total body PET," EJNMMI Phys, vol. 7, no. 1, p. 35, Dec. 2020, doi: 10.1186/s40658-020-00290-2.

[10] X. Zhang, J. Zhou, S. R. Cherry, R. D. Badawi, and J. Qi, "Quantitative image reconstruction for total-body PET imaging using the 2-meter long EXPLORER scanner," Phys. Med. Biol., vol. 62, no. 6, pp. 2465–2485, Mar. 2017, doi: 10.1088/1361-6560/aa5e46.

[11] R. D. Badawi et al., "First Human Imaging Studies with the EXPLORER Total-Body PET Scanner*," J Nucl Med, vol. 60, no. 3, pp. 299–303, Mar. 2019, doi: 10.2967/jnumed.119.226498.

[12] M. Conti, "Focus on time-of-flight PET: the benefits of improved time resolution," Eur J Nucl Med Mol Imaging, vol. 38, no. 6, pp. 1147–1157, Jun. 2011, doi: 10.1007/s00259-010-1711-y.

[13] P. Lecoq et al., "Roadmap toward the 10 ps time-of-flight PET challenge," Phys. Med. Biol., vol. 65, no. 21, p. 21RM01, Oct. 2020, doi: 10.1088/1361-6560/ab9500.

[14] J. Van Sluis et al., "Performance Characteristics of the Digital Biograph Vision PET/CT System," J Nucl Med, vol. 60, no. 7, pp. 1031–1036, Jul. 2019, doi: 10.2967/jnumed.118.215418.

[15] M. S. Lee, J. W. Cates, A. Gonzalez-Montoro, and C. S. Levin, "High-resolution time-of-flight PET detector with 100 ps coincidence time resolution using a side-coupled phoswich configuration," Phys. Med. Biol., vol. 66, no. 12, p. 125007, Jun. 2021, doi: 10.1088/1361-6560/ac01b5.

[16] S. I. Kwon et al., "Ultrafast timing enables reconstruction-free positron emission imaging," Nat. Photon., vol. 15, no. 12, pp. 914–918, Dec. 2021, doi: 10.1038/s41566-021-00871-2.

[17] M. Ito, S. J. Hong, and J. S. Lee, "Positron emission tomography (PET) detectors with depth-of- interaction (DOI) capability," Biomed. Eng. Lett., vol. 1, no. 2, pp. 70–81, May 2011, doi: 10.1007/s13534-011-0019-6.

[18] M. Pizzichemi et al., “On light sharing TOF-PET modules with depth of interaction and 157 ps FWHM coincidence time resolution,” Phys. Med. Biol., vol. 64, no. 15, p. 155008, Aug. 2019, doi: 10.1088/1361-6560/ab2cb0.

[19] C. L. Melcher, “Scintillation crystals for PET,” J Nucl Med, vol. 41, no. 6, pp. 1051–1055, Jun. 2000.

[20] M. Korzhik et al., “Development of scintillation materials for PET scanners,” Nuclear Instruments and Methods in Physics Research Section A: Accelerators, Spectrometers, Detectors and Associated Equipment, vol. 571, no. 1–2, pp. 122–125, Feb. 2007, doi: 10.1016/j.nima.2006.10.044.

[21] P. Moskal et al., “Test of a single module of the J-PET scanner based on plastic scintillators,” Nuclear Instruments and Methods in Physics Research Section A: Accelerators, Spectrometers, Detectors and Associated Equipment, vol. 764, pp. 317–321, Nov. 2014, doi: 10.1016/j.nima.2014.07.052.

[22] A. J. Reader and H. Zaidi, “Advances in PET Image Reconstruction,” PET Clinics, vol. 2, no. 2, pp. 173–190, Apr. 2007, doi: 10.1016/j.cpet.2007.08.001.

[23] A. J. Reader, G. Corda, A. Mehranian, C. D. Costa-Luis, S. Ellis, and J. A. Schnabel, “Deep Learning for PET Image Reconstruction,” IEEE Trans. Radiat. Plasma Med. Sci., vol. 5, no. 1, pp. 1–25, Jan. 2021, doi: 10.1109/TRPMS.2020.3014786.

[24] B. A. Spencer et al., “Performance Evaluation of the uEXPLORER Total-Body PET/CT Scanner Based on NEMA NU 2-2018 with Additional Tests to Characterize PET Scanners with a Long Axial Field of View,” J Nucl Med, vol. 62, no. 6, pp. 861–870, Jun. 2021, doi: 10.2967/jnumed.120.250597.

[25] H. J. Frisch, E. J. Oberla, H.-J. Kim, and M. Yeh, “Positron-emission tomography detector systems based on low-density liquid scintillators and precise time-resolving photodetectors,” 10,132,942, Nov. 20, 2018 [Online]. Available: https://www.osti.gov/biblio/1531371

[26] J. F. Shida et al., “Low-dose high-resolution TOF-PET using ionization-activated multi-state low-Z detector media,” Nuclear Instruments and Methods in Physics Research Section A: Accelerators, Spectrometers, Detectors and Associated Equipment, vol. 1017, p. 165801, Nov. 2021, doi: 10.1016/j.nima.2021.165801.

[27] C. Aberle, A. Elagin, H. J. Frisch, M. Wetstein, and L. Winslow, “Measuring directionality in double-beta decay and neutrino interactions with kiloton-scale scintillation detectors,” J. Inst., vol. 9, no. 06, pp. P06012–P06012, Jun. 2014, doi: 10.1088/1748-0221/9/06/P06012.

[28] B. W. Adams et al., “Timing characteristics of Large Area Picosecond Photodetectors,” Nuclear Instruments and Methods in Physics Research Section A: Accelerators, Spectrometers, Detectors and Associated Equipment, vol. 795, pp. 1–11, Sep. 2015, doi: 10.1016/j.nima.2015.05.027.

[29] B. W. Adams et al., “A Brief Technical History of the Large-Area Picosecond Photodetector (LAPPD) Collaboration.” arXiv, Mar. 06, 2016. Accessed: May 05, 2023. [Online]. Available: http://arxiv.org/abs/1603.01843

[30] E. Oberla, J.-F. Genat, H. Grabas, H. Frisch, K. Nishimura, and G. Varner, “A 15GSa/s, 1.5GHz bandwidth waveform digitizing ASIC,” Nuclear Instruments and Methods in Physics Research Section A: Accelerators, Spectrometers, Detectors and Associated Equipment, vol. 735, pp. 452–461, Jan. 2014, doi: 10.1016/j.nima.2013.09.042.

[31] M. J. Berger et al., “XCOM: Photon Cross Section Database (version 1.5).” National Institute of Standards and Technology, Gaithersburg, MD, 2010. [Online]. Available: http://physics.nist.gov/xcom

[32] C. Grignon et al., “Nuclear medical imaging using β+γ coincidences from 44Sc radio-nuclide with liquid xenon as detection medium,” Nuclear Instruments and Methods in Physics Research Section A: Accelerators, Spectrometers, Detectors and Associated Equipment, vol. 571, no. 1–2, pp. 142–145, Feb. 2007, doi: 10.1016/j.nima.2006.10.048.

[33] E. Yoshida et al., “Whole gamma imaging: a new concept of PET combined with Compton imaging,” Phys. Med. Biol., vol. 65, no. 12, p. 125013, Jun. 2020, doi: 10.1088/1361-6560/ab8e89.

[34] K. Matsuda and M. Irie, “Diarylethene as a photoswitching unit,” Journal of Photochemistry and Photobiology C: Photochemistry Reviews, vol. 5, no. 2, pp. 169–182, Oct. 2004, doi: 10.1016/S1389-5567(04)00023-1.

[35] R. Iwai, M. Morimoto, and M. Irie, “Turn-on mode fluorescent diarylethenes: effect of electron-donating and electron-withdrawing substituents on photoswitching performance†,” Photochem Photobiol Sci, vol. 19, no. 6, pp. 783–789, Jun. 2020, doi: 10.1039/d0pp00064g.

[36] M. Irie, Diarylethene molecular photoswitches: concepts and functionalities. Weinheim: Wiley-VCH, 2021.

[37] J. Perl, J. Shin, J. Schümann, B. Faddegon, and H. Paganetti, “TOPAS: An innovative proton Monte Carlo platform for research and clinical applications: TOPAS: An innovative proton Monte Carlo platform,” Med. Phys., vol. 39, no. 11, pp. 6818–6837, Oct. 2012, doi: 10.1118/1.4758060.

[38] S. Agostinelli et al., “Geant4—a simulation toolkit,” Nuclear Instruments and Methods in Physics Research Section A: Accelerators, Spectrometers, Detectors and Associated Equipment, vol. 506, no. 3, pp. 250–303, Jul. 2003, doi: 10.1016/S0168-9002(03)01368-8.

[39] J. Allison et al., “Geant4 developments and applications,” IEEE Trans. Nucl. Sci., vol. 53, no. 1, pp. 270–278, Feb. 2006, doi: 10.1109/TNS.2006.869826.

[40] J. Allison et al., “Recent developments in Geant4,” Nuclear Instruments and Methods in Physics Research Section A: Accelerators, Spectrometers, Detectors and Associated Equipment, vol. 835, pp. 186–225, Nov. 2016, doi: 10.1016/j.nima.2016.06.125.

[41] J. Baró, J. Sempau, J. M. Fernández-Varea, and F. Salvat, “PENELOPE: An algorithm for Monte Carlo simulation of the penetration and energy loss of electrons and positrons in matter,” Nuclear Instruments and Methods in Physics Research Section B: Beam Interactions with Materials and Atoms, vol. 100, no. 1, pp. 31–46, May 1995, doi: 10.1016/0168-583X(95)00349-5.

[42] Nuclear Energy Agency, PENELOPE 2018: A code system for Monte Carlo simulation of electron and photon transport: Workshop Proceedings, Barcelona, Spain, 28 January – 1 February 2019. in PENELOPE: A code system for Monte Carlo simulation of electron and photon transport. OECD, 2019. doi: 10.1787/32da5043-en.

[43] “PETRELAB 550-Q - C10-C13 Linear Alkylbenzene (LAB): Technical Data Sheet.” CEPSA, 2022. Accessed: May 05, 2023. [Online]. Available: https://chemicals.cepsa.com/en/chemical-products/petrelab-550-q

[44] Geant4 Collaboration, User’s Guide for Application Developers using the Geant4 toolkit v. 11.1 (doc Rev7.0) - Appendix: Geant4 Material Database. Geneva, Switzerland: CERN, 2022. [Online]. Available: https://geant4-userdoc.web.cern.ch/UsersGuides/ForApplicationDeveloper/html/Appendix/materialNames.html

[45] S. E. Derenzo, “Monte Carlo simulations of time-of-flight PET with double-ended readout: calibration, coincidence resolving times and statistical lower bounds,” Phys. Med. Biol., vol. 62, no. 9, pp. 3828–3858, May 2017, doi: 10.1088/1361-6560/aa6862.

[46] W. P. Segars, G. Sturgeon, S. Mendonca, J. Grimes, and B. M. W. Tsui, “4D XCAT phantom for multimodality imaging research: 4D XCAT phantom for multimodality imaging research,” Med. Phys., vol. 37, no. 9, pp. 4902–4915, Aug. 2010, doi: 10.1118/1.3480985.

[47] K. Domurat-Sousa et al., “TOPAS Simulation of a Low-Z TOF-PET Scanner (Version 1.0.0).” University of Chicago, 2023. [Online]. Available: https://github.com/squireslab/low_z_pet_scanner

[48] S. DeBenedetti, C. E. Cowan, W. R. Konneker, and H. Primakoff, “On the Angular Distribution of Two-Photon Annihilation Radiation,” Phys. Rev., vol. 77, no. 2, pp. 205–212, Jan. 1950, doi: 10.1103/PhysRev.77.205.

[49] C. S. Levin and E. J. Hoffman, “Calculation of positron range and its effect on the fundamental limit of positron emission tomography system spatial resolution,” Phys. Med. Biol., vol. 44, no. 3, pp. 781–799, Mar. 1999, doi: 10.1088/0031-9155/44/3/019.

[50] A. Blanco, “Positron Range Effects on the Spatial Resolution of RPC-PET,” in 2006 IEEE Nuclear Science Symposium Conference Record, San Diego, CA: IEEE, Oct. 2006, pp. 2570–2573. doi: 10.1109/NSSMIC.2006.354433.

[51] Geant4 Collaboration, User’s Guide: Physics Reference Manual for Geant4 toolkit v. 11.1 (doc Rev7.0). Geneva, Switzerland: CERN, 2022. [Online]. Available: https://geant4-userdoc.web.cern.ch/UsersGuides/PhysicsReferenceManual/html/index.html

[52] W. M. Haynes, Ed., CRC Handbook of Chemistry and Physics, 0 ed. CRC Press, 2014. doi: 10.1201/b17118.

[53] O. Klein and Y. Nishina, “The Scattering of Light by Free Electrons according to Dirac’s New Relativistic Dynamics,” Nature, vol. 122, no. 3072, pp. 398–399, Sep. 1928, doi: 10.1038/122398b0.

[54] NEMA Standards Publication NU 2-2018: Performance Measurements of Positron Emission Tomographs (PETS). Rosslyn, VA: National Electrical Manufacturers Association, 2018. [Online]. Available: http://wwww.nema.org

[55] M. P. W. Chin, T. T. Böhlen, A. Fassò, A. Ferrari, P. G. Ortega, and P. R. Sala, “FLUKA and PENELOPE simulations of 10keV to 10MeV photons in LYSO and soft tissue,” Radiation Physics and Chemistry, vol. 95, pp. 170–173, Feb. 2014, doi: 10.1016/j.radphyschem.2013.03.024.

[56] X. Yu et al., “Requirements of Scintillation Crystals with the Development of PET Scanners,” Crystals, vol. 12, no. 9, p. 1302, Sep. 2022, doi: 10.3390/cryst12091302.

[57] C. H. Clement and International Commission on Radiological Protection, Eds., Adult reference computational phantoms: joint ICRP/ICRU report. in Annals of the ICRP, no. 39.2009,2. Amsterdam: Elsevier, 2009.

[58] C. H. Kim et al., Adult mesh-type reference computational phantoms. in Annals of the ICRP, no. volume 49, no. 3 (2020). London: SAGE, 2020.

[59] International Commission on Radiation Units and Measurements, “Photon, Electron, Proton and Neutron Interaction Data for Body Tissues,” International Commission on Radiation Units and Measurements, Bethesda, MD, USA, 1992. [Online]. Available: https://www.osti.gov/biblio/7114520

[60] E. E. Verwer et al., “Harmonisation of PET/CT contrast recovery performance for brain studies,” Eur J Nucl Med Mol Imaging, vol. 48, no. 9, pp. 2856–2870, Aug. 2021, doi: 10.1007/s00259-021-05201-w.

[61] J. Lee, S. Oya, and B. Sade, “Benefits and limitations of diameter measurement in the conservative management of meningiomas,” Surg Neurol Int, vol. 2, no. 1, p. 158, 2011, doi: 10.4103/2152-7806.89857.